Improved ultrasound image quality with pixel-based beamforming using a Wiener-filter and a SNR-dependent coherence factor

Hui-Wen Xie[a,#], Hao Guo[a,#], Guang-Quan Zhou[a,*], Nghia Q. Nguyen[b,c] and Richard W. Prager[b,c]

[a] *The School of Biological Science and Medical Engineering, Southeast University, Nanjing, China*
[b] *Department of Engineering, University of Cambridge, Cambridge CB2 1PZ, UK*
[c] *Cambridge University - Nanjing Centre of Technology and Innovation, Nanjing, China*

ARTICLE INFO

Keywords:
Ultrasound beamforming
Pixel-based
Wiener-filter
Axial resolution
Coherence factor
Image quality

ABSTRACT

Pixel-based beamforming generates focused data by assuming that the waveforms received on a linear transducer array are composed of spherical pulses. It does not take into account the spatiotemporal spread in the data from the length of the excitation pulse or from the transfer functions of the transducer elements. As a result, these beamformers primarily have impacts on lateral, rather than axial, resolution. This paper proposes an efficient method to improve the axial resolution for pixel-based beamforming. We extend our field pattern analysis and show that the received waveforms should be passed through a Wiener filter before being used in the coherent pixel-based beamformer. This filter is designed based on signals echoed from a single scatterer at the transmit focus. The beamformer output is then combined with a *coherence factor*, that is adaptive to the signal-to-noise ratio, to improve the image contrast and suppress artifacts that have arisen during the filtering process. We validate the proposed method and compare it with other beamforming strategies using a series of experiments, including simulation, phantom and *in vivo* studies. It is shown to offer significant improvements in axial resolution and contrast over coherent pixel-based beamforming, as well as other spatial filters derived from synthetic aperture imaging. The method also demonstrates robustness to modeling errors in the experimental data. Overall, the imaging results show that the proposed approach has the potential to be of value in clinical applications.

1. Introduction

Advances in high-performance computing and hardware flexibility have resulted in the development of increasingly complex beamformers with focussing in both transmit and receive directions [1]. Prominent among these systems is the *synthetic aperture* (SA) approach using diverging wave on transmit [2]. The data is extracted by using the time delay, calculated based on the spherical assumption of the transmit wave-shape. SA imaging has been shown to improve image quality. Most of its impact, however, is on the lateral resolution which benefits directly from the large “synthesized” aperture.

In previous studies [3, 4], we developed similar beamformers based on conventional pulse-echo sequences with focused transmits. Instead of assuming the transmit wave-shape to be a spherical pulse as in other studies [5, 6, 7], we analyzed the field pattern and found that it was better described by a superposition of two spherical pulses. The pulse timings correspond to the minimal and maximal distances from the imaging point to the transmit subaperture. Based on our new description of the wave-shape, we developed algorithms to select the best possible signals associated with these pulses for calculating the beamformed data. The B-mode image is created with high and uniform resolution over the entire imaging region. We named these methods *pixel-based* (PB) beamformers implying the data is generated at individual pixels of the imaging region [3]. Like for the SA imaging, however, the major improvements offered by the PB beamformers are in the lateral resolution. Extending these methods to improve the axial resolution is the main purpose of this work.

Attempts to improve the axial resolution usually lead to the use of deconvolution[8], or *spatiotemporal 2-D Wiener filters*, applied to the beamformed radio-frequency (RF) data. The RF data is assumed to be the output of a linear shift-invariant system. It is modeled as a 2-D linear convolution between the system *point-spread-function* (psf) and the scattering field. Because of ultrasound attenuation and the way the beam shape varies with depth, the shape of the

---

These two authors contributed equally to this work.
ORCID(s):

psf changes significantly as a function of the distance from the probe face. The ultrasound system is thus linear-shift-variant [9] in the axial direction. Success in this deconvolution depends strongly on knowledge of the psf and working on a small enough region for the shift-invariant approximation to be reasonable.

In [10, 11], we developed 2-D Wiener filters that either handled the shift-variance directly or divided the imaging region into multiple *isoplanatic* patches. In the second case, the Wiener filters were performed locally with the psf updated within each patch. This improves the image resolution, albeit at a high computational cost. Another method is *blind deconvolution* where the image and psf are reconstructed simultaneously [12, 13]. However, it is usually based on statistical assumptions which may not be followed by the real data. Recently, deconvolution has been combined with l_1-norm regularization to form sparse reconstructions for ultrasound imaging [14]. In these complex algorithms, the quality of reconstructed images is still potentially affected by errors caused by assumptions about the point-spread function.

In another approach, the image quality can be increased by applying a matched filter to the received waveforms before the beamforming process [15, 16, 17]. This was first proposed for SA imaging by Jensen and Gori in [15]. The principle of the matched filter is to emphasize the time-series signals that are echoed from individual points-of-interests. The work is applied to the diverging wave and found to improve the lateral resolution in simulations. On *in vivo* data, however, the improvement became less obvious. The matched filter was also extended to data acquired with focused beams in [17]. It was shown to enhance the echo signal-to-noise ratio at the cost of axial resolution. Upgrading to a Wiener filter was suggested as a way to further increase the sharpness of the focused image [15].

In this paper, we develop a filtering strategy for improving the axial resolution of PB beamforming that is efficient in terms of both computation and system architecture. In Section 2, we extend our field pattern analysis and show that the received waveforms can be deconvolved using signals obtained by scanning a single scatterer at the transmit focus. The filtering process is performed before the coherent delay-and-sum [4]. We then draw on other studies and apply the SNR-dependent coherence factor (SNRD-CF) as a post-processing filter to the beamformer output [18]. This helps to suppress the artifacts arising from the filtering process and to enhance the imaging contrast. Our method is validated and evaluated in Section 3 on a series of datasets, including simulations [19] and experiments with the Vantage 256 system (Verasonics, Inc., Kirkland, WA, USA). The results are discussed in Section 4. Finally, we summarize our work in Section 5.

2. Methods

In our study, the beamforming methods are developed based on the field pattern analysis [3, 4]. In this section, we briefly summarize the analysis from which the coherent PB beamforming is derived. Details of the analysis can be found in [3, 4]. We then show how to combine the coherent PB algorithm with a Wiener filter as a pre-beamforming filter and a coherence factor as a post-beamforming filter to enhance the image quality.

2.1. Field Pattern Analysis

We begin with the popular expression for a pressure field arriving at imaging point P [19], given by

$$p\left(\mathbf{x}_p, t\right) = \rho v(t) \underset{t}{*} \frac{\partial h_t(\mathbf{x}_p, t)}{\partial t} , \tag{1}$$

where $\mathbf{x}_p$ is the position vector of P, $v(t)$ is a sinusoidal and uniform excitation on transmit, ρ is the equilibrium density of the weakly-scattering medium, $h_t\left(\mathbf{x}_p, t\right)$ is the transmit spatial impulse response, and $\underset{t}{*}$ denotes temporal convolution. By taking the transmit delay into account, we can approximate the transmit subaperture as a continuous arc focused at point F and calculate $\partial h_t(\mathbf{x}_p, t)/\partial t$ by [4]

$$\begin{aligned} \frac{\partial h_t\left(\mathbf{x}_p, t\right)}{\partial t} \approx & \frac{c\beta_{min}}{2\pi}\delta\left(t - \frac{R_{min}}{c}\right) \\ & - \frac{c\beta_{max}}{2\pi}\delta\left(t - \frac{R_{max}}{c}\right) , \end{aligned} \tag{2}$$

where R_{min} and R_{max} are the minimal and maximal distances from P to the aperture, c is the sound-speed, and β_{min} and β_{max} are angular coefficients respectively associated with those distances. By substituting Eq. (2) into (1), we can

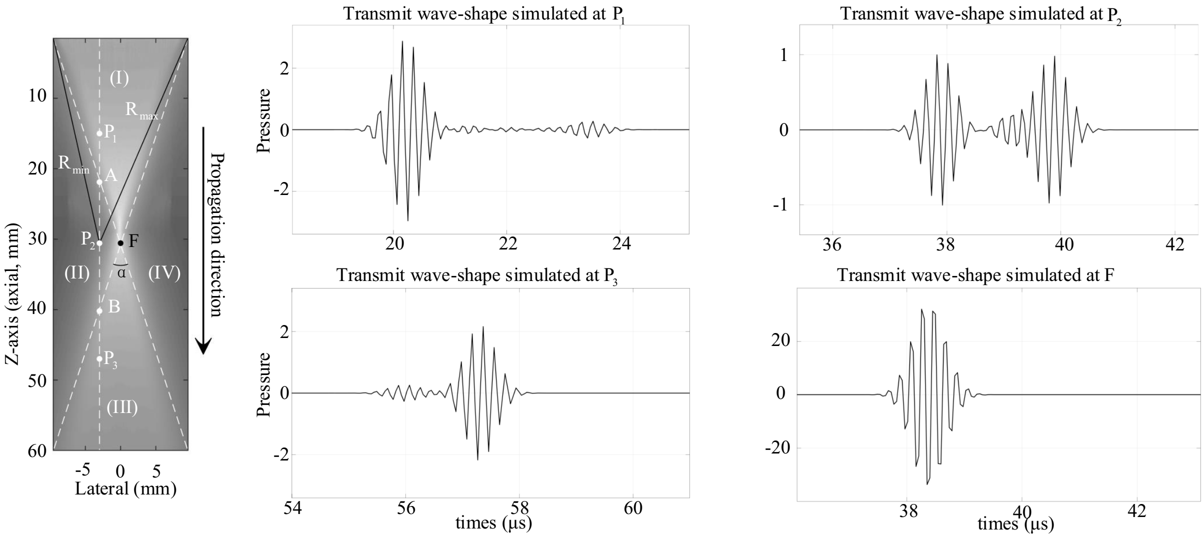

(a)

(b)

Fig. 1: (a) The transmit field pattern simulated with Field II based on the parameters of the Vantage 256 system with Philips L7-4 probe. (b) Transmit waveshapes generated at imaging points P_1, P_2, P_3, and the focus F. All waveshapes are normalized to the amplitude of that at P_2 [4].

show that the transmit wave-shape may be described by the superposition of two spherical pulses corresponding to R_{min} and R_{max}. The two pulses have relative magnitudes that vary depending on the position of P in the insonified region.

Fig. 1(a) shows the field pattern of a transmit beam focused at F. It is simulated based on the parameters of the Vantage 256 system using Field II (see the system description in Section. 3.1). By defining α as a limited angle, or the angle-of-view from F to the transmit subaperture, it divides the image plane into four regions, denoted (I) to (IV) counterclockwise. Fig. 1(b) shows the transmit waveshapes generated at an imaging point from each of the four regions. For P in region (I), the first pulse dominates the transmit waveform. In region (III), however, the second pulse becomes dominant. In regions (II) and (IV), the two pulses are of more similar magnitude. At the focus F, the two pulses are merged with each other, and have the largest amplitude.

The two-pulse model for the transmit wave-shape in our study is a generalization of the virtual-source-element (VSE) technique. In the VSE approach, the source is assumed to exist at the focus and a spherical wave is considered to propagate back and forth from this point [20]. This, however, is only valid within the limited angle α, i.e., inside regions (I) and (III). In regions (II) and (IV), the VSE becomes a poor approximation. Without an appropriate algorithm to process data in this region, the resulting B-mode image has artifacts that cannot be easily corrected [21]. Based on the two-pulse model, we have developed several PB beamforming strategies that generate B-mode images with high-resolution and a smooth transition in regions (II) and (IV). In the next section, we summarize our most recent approach – the coherent PB beamformer, which was presented in [4].

2.2. Coherent Pixel-Based Beamformer

The coherent PB beamformer combines the high-energy signals associated with the two pulses to generate focused data. Signals are extracted from the received waveforms using time-delay calculations. Details of the calculations are provided in [4]. At each transmit, the imaging equation of the coherent PB algorithm is given by

$$g(\mathbf{x}_p) = \sum_{j}^{N_r} w_j \left(c_1 r_j(t)\,|_{t=\tau_{p,min}} + c_2 r_j(t)\,|_{t=\tau_{p,max}} \right) , \tag{3}$$

where N_r is the number of receiving elements per transmit, $r_j(t)$ is the waveform or echo RF trace received on element j, $\tau_{p,min}$ and $\tau_{p,max}$ are the time-delays associated with the two pulses in the transmit wave-shape. Definitions for w_j, c_1 and c_2 are given below. The focused data is generated by compounding $g(\mathbf{x}_p)$ over a large number of overlapped transmits.

A particular feature of the coherent PB in contrast to other beamforming methods is that it can extract up to two signals from each received waveform to generate $g(\mathbf{x}_p)$. These signals, however, must be compounded coherently based on the field pattern analysis. The weights w_j are used to suppress the noise from regions far from the beam centreline, while coefficients $\left(c_1, c_2\right)$ are selected based on the image region: (I)–(IV).

In particular, for P in (I) and (III) where one pulse dominates the other, we select the data with the higher magnitude pulses only. Thus, $\left(c_1, c_2\right) = (1, 0)$ for P in region (I) and $\left(c_1, c_2\right) = (0, -1)$ for P in region (III). The minus sign is because of the opposite phases between the two pulses (see Fig. 1(b)). In region (II) (and similarly in region (IV)), we choose $\left(c_1, c_2\right)$ for P by using

$$c_1 = \frac{|\mathbf{x}_b - \mathbf{x}_p|}{|\mathbf{x}_b - \mathbf{x}_a|} \quad \text{and} \quad c_2 = -\frac{|\mathbf{x}_a - \mathbf{x}_p|}{|\mathbf{x}_a - \mathbf{x}_b|} \ , \tag{4}$$

where $\mathbf{x}_a$, $\mathbf{x}_b$, and $\mathbf{x}_p$ are the position vectors of A, B, and P (see Fig. 1(a)). Notice the minus sign for c_2, again, to account for the phase opposition between the two pulses.

This strategy can still be classified as a delay-and-sum beamformer. It is performed without any filtering process. In the next section, we exploit filters that can be incorporated with this strategy to enhance the image focusing.

2.3. Spatial Filters for Image Focusing

We first introduce the matched filter from SA imaging which can be applied to pixel-based beamforming [15]. It is also developed based on the field pattern analysis. A signal $r_{j,\mathrm{P}}\,(t)$, reflected from an imaging point P and received on element j, can be written as

$$r_{j,\mathrm{P}}\,(t) = \frac{\rho}{2c^2} E_m(t) \underset{t}{*} \frac{\partial^3 v(t)}{\partial t^3} \underset{t}{*} f_m\left(\mathbf{x}_p\right) \underset{\mathbf{x}}{*} h_{pe}\left(\mathbf{x}_p, \mathbf{x}_j, t\right) \ , \tag{5}$$

where $E_m(t)$ is the electro-mechanical impulse response from transducer force to voltage during reception, $f_m\left(\mathbf{x}_p\right)$ accounts for the inhomogeneities in the soft tissue, $\mathbf{x}_j$ is the position vector of receiving element j, $h_{pe}\left(\mathbf{x}_p, \mathbf{x}_j, t\right)$ is the pulse-echo spatial impulse response, and $\underset{\mathbf{x}}{*}$ is spatial convolution.

The matched filter is formed by using the signal reflected from a single scatterer at the same position, given by

$$\begin{aligned} m_p\left(\mathbf{x}_p, \mathbf{x}_j, t\right) &= p_r\left(\mathbf{x}_p, \mathbf{x}_j, -t\right) \quad \text{where} \\ p_r\left(\mathbf{x}_p, \mathbf{x}_j, t\right) &= \frac{\rho}{2c^2} E_m(t) \underset{t}{*} \frac{\partial^3 v(t)}{\partial t^3} \underset{t}{*} h_{pe}\left(\mathbf{x}_p, \mathbf{x}_j, t\right) \ . \end{aligned} \tag{6}$$

in which $m_p\left(\mathbf{x}_p, \mathbf{x}_j, t\right)$ is the matched filter impulse response, $p_r\left(\mathbf{x}_p, \mathbf{x}_j, t\right)$ is obtained from (5) by replacing $f_m\left(\mathbf{x}_p\right)$ with a spatial delta function.

Data obtained from $r_j(t)$ through the matched filter is calculated by

$$r_{j,\mathrm{P}}^{\mathrm{MF}} = \int_{\tau_0-\Delta T/2}^{\tau_0+\Delta T/2} r_j\,(t)\, m_p\left(\mathbf{x}_p, \mathbf{x}_j, -t\right)\ dt \ , \tag{7}$$

where τ_0 is the center of the response, and ΔT is the duration of the matched filter.

In Eq. (7), the output $r_{j,\mathrm{P}}^{\mathrm{MF}}$ does not depend on τ_0, as long as $m_p\left(\mathbf{x}_p, \mathbf{x}_j, t\right)$ is within the interval from $\tau_0 - \Delta T/2$ to $\tau_0 + \Delta T/2$. For convenience, we choose τ_0 based on the distance from the transmit subaperture center to the imaging point P and back to the received element j, and set ΔT long enough so that the interval $\left[\tau_0 - \Delta T/2, \tau_0 + \Delta T/2\right]$ covers the entire pulse $m_p\left(\mathbf{x}_p, \mathbf{x}_j, t\right)$. This strategy is equivalent to the *conventional PB beamformer* (see [3]) but incorporates a matched filter before the data migration. We name it the *spatial-matched-filter pixel-based* (SMF-PB) beamformer.

We also follow the suggestions in [15] that upgrade the matched filter to the Wiener filter. The pulse $m_p\left(\mathbf{x}_p, \mathbf{x}_j, t\right)$ in (7) is replaced by a response from the deconvolution. The Wiener filter response can be calculated in the frequency domain, given by

$$W\left(\mathbf{x}_p, \mathbf{x}_j, \omega\right) = \frac{M^*\left(\mathbf{x}_p, \mathbf{x}_j, \omega\right)}{\left|M\left(\mathbf{x}_p, \mathbf{x}_j, \omega\right)\right|^2 + \Gamma} \ , \tag{8}$$

where $M\left(\mathbf{x}_p, \mathbf{x}_j, \omega\right)$ is the Fourier transform of $m_p\left(\mathbf{x}_p, \mathbf{x}_j, t\right)$, $M^*\left(\mathbf{x}_p, \mathbf{x}_j, \omega\right)$ is its complex conjugate, and Γ is a constant ratio between the squared spectrum of noise and that of the signal [12]. In practice, however, Γ is estimated from the recorded data. We name this method the *spatial-Wiener-filter pixel-based* (SWF-PB) beamformer.

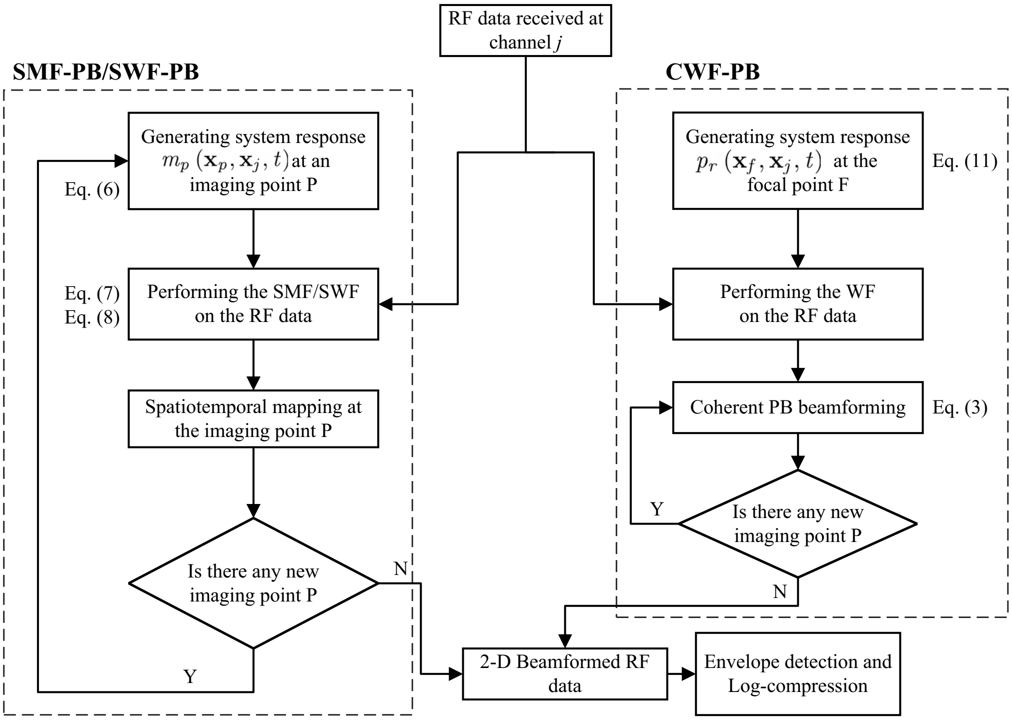

Fig. 2: The block diagram of the SMF-PB/SWF-PB beamformer and the CWF-PB beamformer.

2.4. Coherent Wiener-filter Pixel-Based Beamformer

We propose a new Wiener filter by extending the field pattern analysis. First, we separate $h_{pe}\left(\mathbf{x}_p, \mathbf{x}_j, t\right) = h_t\left(\mathbf{x}_p, t\right) \underset{t}{*} h_r\left(\mathbf{x}_p, \mathbf{x}_j, t\right)$, where h_t and h_r are the transmit and receive spatial impulse response respectively. The signal reflected from P and received by element j can be re-written from (5) as

$$\begin{aligned} r_{j,\mathrm{P}}(t) &= \frac{\rho}{2c^2} E_m(t) \underset{t}{*} \frac{\partial^2 v(t)}{\partial t^2} \underset{t}{*} f_m\left(\mathbf{x}_p\right) \\ &\underset{\mathbf{x}}{*} \frac{\partial h_t\left(\mathbf{x}_p, t\right)}{\partial t} \underset{t}{*} h_r\left(\mathbf{x}_p, \mathbf{x}_j, t\right) . \end{aligned} \tag{9}$$

In Eq. (9), $h_r\left(\mathbf{x}_p, \mathbf{x}_j, t\right)$ is the spatial impulse response that describes the wave propagation from P to receive element j. By ignoring the directivity of this element, we can assume that the shape of $h_r\left(\mathbf{x}_p, \mathbf{x}_j, t\right)$ is independent of P. From Eq. (2), we find at the focus F:

$$\frac{\partial h_t\left(\mathbf{x}_f, t\right)}{\partial t} \approx \frac{c\beta_0}{2\pi} \delta\left(t - \frac{R_0}{c}\right) , \tag{10}$$

where $\mathbf{x}_f$ is the position of F, R_0 is the radius of the transmit subaperture, and β_0 is the angular coefficient associated with the pulse. This is illustrated in the last plot of Fig. 1(b) where the two pulses in the transmit wave-shape are merged into one at the focus F. Thus, the received signal from a single scatterer at F is given by

$$p_r\left(\mathbf{x}_f, \mathbf{x}_j, t\right) = v_{pe}(t) \underset{t}{*} \delta\left(t - \frac{R_0}{c}\right) \underset{t}{*} h_r\left(\mathbf{x}_f, \mathbf{x}_j, t\right) , \tag{11}$$

where $v_{pe}(t) \cong E_m(t) \underset{t}{*} \partial^2 v(t)/\partial t^2$.

By assuming $h_r\left(\mathbf{x}_f, \mathbf{x}_j, t\right)$ and $h_r\left(\mathbf{x}_p, \mathbf{x}_j, t\right)$ have the same shape, $p_r\left(\mathbf{x}_f, \mathbf{x}_j, t\right)$ in (11) can be used to deconvolve $r_{j,\mathrm{P}}(t)$ to suppress the effects of $v_{pe}(t)$ and $h_r\left(\mathbf{x}_p, \mathbf{x}_j, t\right)$. This argument is valid for every imaging point P in the imaging region. Thus, we can use $p_r\left(\mathbf{x}_f, \mathbf{x}_j, t\right)$ as a kernel to deconvolve the entire received waveform $r_j(t)$. Since $\partial h_t\left(\mathbf{x}_p, t\right)/\partial t$ still varies in the filtered waveforms which is modeled by a sum of two spherical pulses, the coherent PB should be applied after the deconvolution to select and combine the high energy signals associated with the two pulses of $\partial h_t\left(\mathbf{x}_p, t\right)/\partial t$. We name this method the *coherent Wiener-filter pixel-based* (CWF-PB) beamformer. This beamformer, along with the SMF-PB and SWF-PB, are summarized in the block diagrams in Fig. 2.

2.5. SNR-Dependent Postfiltering

A significant challenge when developing a Wiener filter for ultrasound imaging is to extract an accurate psf. There are many uncertain processes inside the ultrasound system and varying factors in the imaging environment making it difficult to calibrate or model the psf precisely. Poor calibration of the psf can result in phase distortion and affect the resolution of final images. In this study, we combine the CWF-PB beamformer with a coherence factor (CF) to further improve the image quality. This factor was originally developed as a metric of focusing quality and calculated as the ratio between the coherent and incoherent sum of an array signal [22], given by

$$w_{CF}(t) = \frac{\left|\sum_{j=1}^{N_\mathrm{r}} r_j(t)\right|^2}{N_\mathrm{r} \sum_{j=1}^{N_\mathrm{r}} \left|r_j(t)\right|^2}, \tag{12}$$

where N_r is the number of receive elements. In [23, 24], it is shown that the CF can be used as a weight coefficient at the output of the delay-and-sum or minimum variance beamformer. It enhances the image quality by reducing the sidelobes caused by phase aberrations. In [25, 26, 27], however, the CF is shown to over-suppress the imaging brightness, which creates artifacts on the generated images.

In this study, we propose to use the Signal-to-Noise-Ratio-Dependent CF (SNRD-CF) [18], a modified version of the CF, given by

$$w_{CF-SNRD}(t) = \frac{w_{CF}(t)}{w_{CF}(t) + \eta(SNR)\left(1 - w_{CF}(t)\right)}, \tag{13}$$

where $w_{CF}(t)$ is given in Eq. (12) and $\eta(SNR)$ is calculated as

$$\eta(SNR) = \frac{N_\mathrm{r} - 1}{2N_\mathrm{r}}\left\{1 - \tanh\left[\alpha\frac{P_s}{P_n} - \beta\right]\right\} + \frac{1}{N_\mathrm{r}}, \tag{14}$$

where P_s and P_n are the low and high frequency components of the signal at individual pixels, α and β are constant parameters.

The coefficient $\eta(SNR)$ is stretched nonlinearly from 0 to 1 as P_s/P_n is varied from 0 to ∞. At a low SNR, P_s/P_n is small and $w_{CF-SNRD}(t)$ acts like the standard $w_{CF}(t)$ in (12) to suppress the noise. At a high SNR, however, P_s/P_n becomes large and $w_{CF-SNRD}(t)$ is close to 1 to maintain the desired signal. The nonlinear variation of the parameter from 0 to 1 helps to alleviate any drastic reductions in imaging brightness[18]. Parameters α and β also help tune the factor to adapt to the generated data. In the CWF-PB beamforming, there are two data vectors extracted for each imaging point in regions (II) and (IV). In this case, the SNRD-CF is performed after the two vectors have been combined.

2.6. Performance Metrics

We evaluate the beamformer performance from the quality of generated images. It is measured using four metrics: spatial resolution, imaging contrast [28], generalized contrast-to-noise ratio (gCNR) [29], and echo signal-to-noise ratio (eSNR).

The spatial resolution can be quantified using the response of each beamformer to individual point-targets in simulation, or wire-targets in a phantom study. In general, the smaller the beamwidth the better the beamformer performance. Although this study focuses on the axial resolution, we still calculated the point target size in the lateral direction for the purposes of reference.

The imaging contrast is evaluated based on a contrast ratio (CR) between a lesion and the background, given by [4]

$$\mathrm{CR} = \frac{\left|I_{out} - I_{in}\right|}{\sqrt{I_{out}^2 + I_{in}^2}}, \tag{15}$$

where I_{in} and I_{out} are the mean intensities measured inside and outside the lesion (in decibels (dB)), respectively. It has a value of 1 for perfect contrast and 0 for no contrast between the lesion and background. To minimise the effect of variations in the attenuation and diffraction of the ultrasound, we choose the kernel as a circular ring enclosing the lesion and with the area equal to that of the lesion (Fig. 3(a)).

Recently, the generalized contrast-to-noise ratio (gCNR) has been proposed as a performance metric to measure the detectability of a lesion from the speckle background, given by [30]

$$\mathrm{gCNR} = 1 - \int \min\left\{p_i(x), p_o(x)\right\} dx, \tag{16}$$

where $p_i(x)$ is the probability density function of the values inside the lesion, and $p_o(x)$ is the probability density function of the values of the background. It has a value that varies from 0 to 1 with increasing lesion detectability. The gCNR metric is shown to be more robust than the contrast or contrast-to-noise ratio metrics towards some image processing transformation such as scale, shift and affine mappings that can alter the dynamic range of the image.

Finally, we employed the eSNR to quantify the penetration, which is given by

$$\mathrm{eSNR} = 10\log_{10}\left(\frac{\mu}{\sigma_{\mathrm{n}}^2}\right), \tag{17}$$

where μ is the ensemble average energy , and σ_n^2 is the noise power of the envelope of beamformed signals. We estimate the echo SNR by using the average/difference over multiple beamformed RF frames of the same scan. It is measured from a kernel that contains no specular reflectors to avoid interference from sidelobes in the noise power.

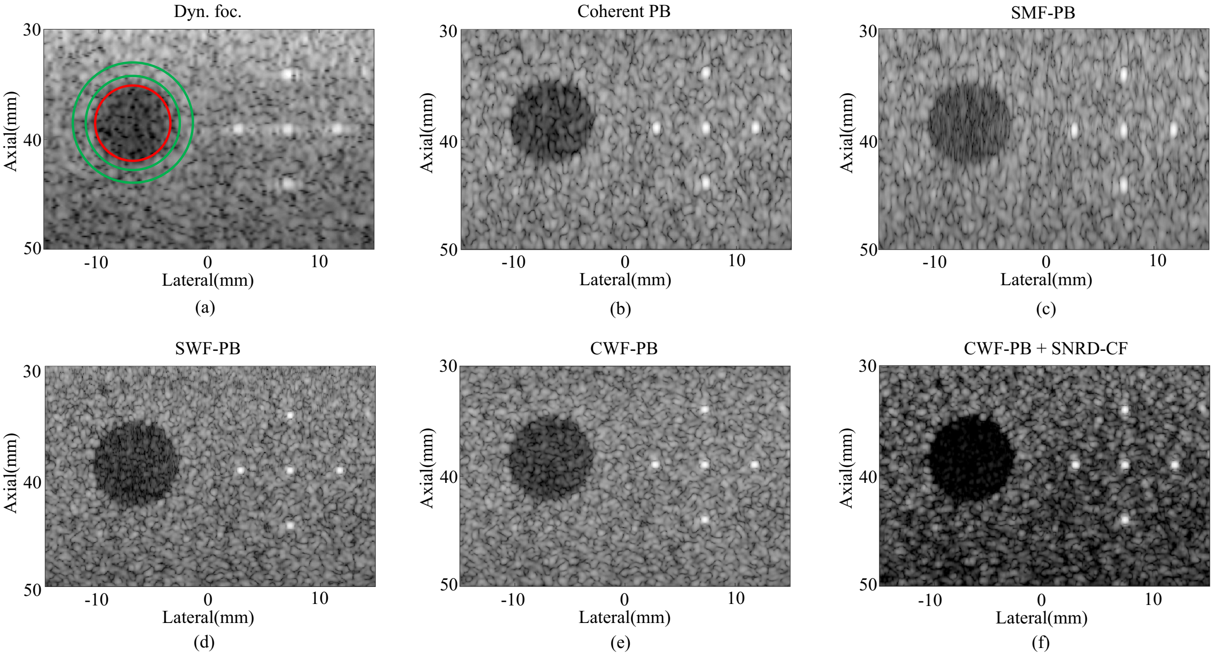

(a) (b) (c) (d) (e) (f)

Fig. 3: Simulated images of a numerical phantom that contains five point-targets and a hypoechoic cyst suspended in a random background. They are generated with different beamformers, including (a) Dynamic focusing (Dyn. foc.), (b) Coherent PB, (c) SMF-PB, (d) SWF-PB, (e) CWF-PB, (f) CWF-PB + SNRD-CF. All pixel-based images are generated with data from 32 transmits. They are log-compressed and displayed with a dynamic range of 70 dB. The regions inside the red circle and between the green rings are the kernels used for the computation of CR and gCNR.

3. Experiments and Results

3.1. Data Acquisition and Processing

In this section, we demonstrate and compare our proposed methods with other beamformers, including the SMF-PB, SWF-PB, and coherent PB. The performance is evaluated on data simulated with the Field II program [19] and on experimental data acquired with the Verasonics Vantage-256 system (Verasonics, Kirkland, WA, USA). We use a 128-element linear array transducer (L7-4, Philips) with 5 MHz central frequency and elevation focus at 25 mm. An excitation voltage is applied to generate an ultrasound pulse-echo with center frequency f_0 of 5.2083 MHz and 67% bandwidth. Data is generated with a 64-element active subaperture on both transmit and receive. It is then sampled at 20.832 MHz, resulting in an axial sampling interval of 0.0370 mm. After each pulse-echo sequence, the transmit beam is shifted by an element pitch of 0.298 mm. We choose to generate the PB images with a five-fold finer grid than the scanning step, equivalent to a 0.0596 mm sampling interval in the lateral direction.

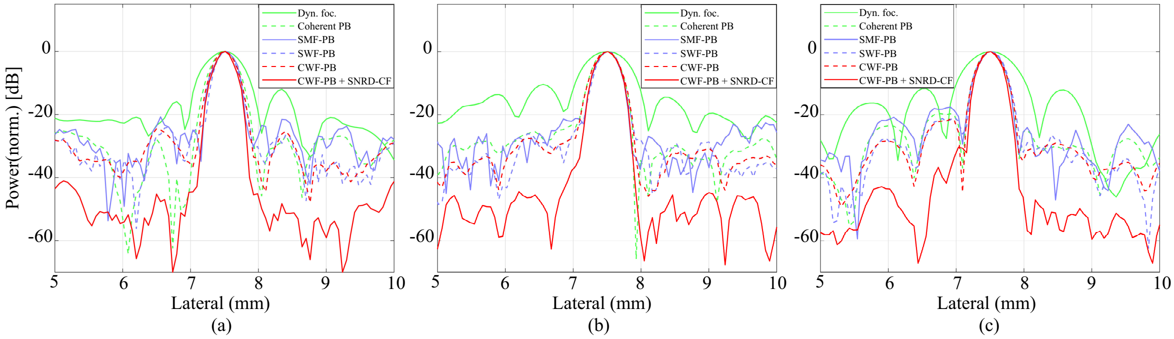

(a)
(b)
(c)

Fig. 4: The lateral responses to the middle point-targets at depths: (a) 34 mm, (b) 39 mm, and (c) 44 mm. They are generated using six beamformers: Dynamic focusing (Dyn. foc.), Coherent PB, SMF-PB, SWF-PB, CWF-PB, and CWF-PB + SNRD-CF.

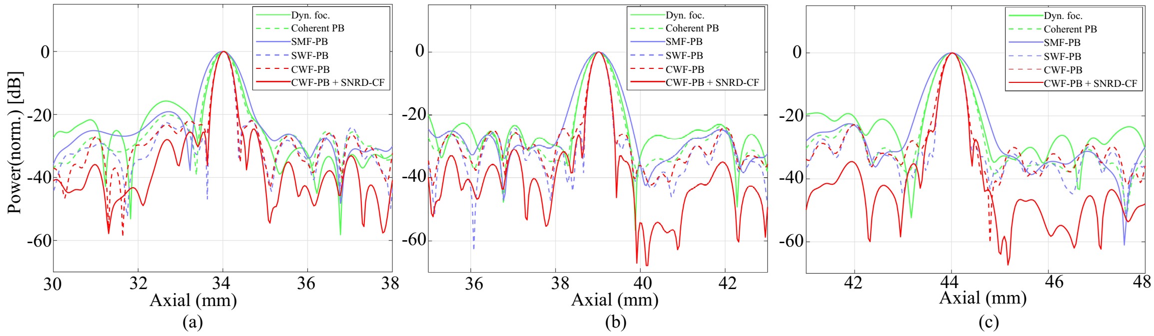

(a)
(b)
(c)

Fig. 5: The axial responses to the middle point-targets at depths: (a) 34 mm, (b) 39 mm, and (c) 44 mm. They are generated using six beamformers: Dynamic focusing (Dyn. foc.), Coherent PB, SMF-PB, SWF-PB, CWF-PB, and CWF-PB + SNRD-CF.

3.2. Simulation

We first evaluate the beamformers on data generated by Field II [19], simulated after the Verasonics system described Section 3.1. A numerical phantom has a circular hypoechoic lesion, 8 mm in diameter and centered at $(z, x) = (39, -6.5)$ mm. There are also five point-targets in the imaging field, arranged in a cross-shape and at depths 34 mm, 39 mm, and 44 mm, with the lateral positions of 3 mm, 7.5 mm, and 12 mm. The transmit focal depth is at 30 mm. The pulses $m_p\left(\mathbf{x}_p, \mathbf{x}_j, t\right)$ and $p_r\left(\mathbf{x}_f, \mathbf{x}_j, t\right)$, used to develop the matched and Wiener filters, are simulated with Field II using the same parameters without considering frequency-dependent attenuation. The value of Γ is empirically set to be 0.5% of the peak value of the data for the WF-based beamformer, while α and β for calculating the SNRD-CF are set to 5 and π, respectively.

Images generated with different beamformers, including Dynamic focusing, are displayed in Figs. 3. Compared to the Dynamic focusing in Fig. 3(a), the coherent PB image in Fig. 3(b) shows much clearer speckle patterns, which indicates a significant improvement in image quality. In our previous study, we have validated the enhancement of coherent PB beamforming on the ULA-OP ultrasound research platform [4, 31]. After applying the matched filter, the generated image (in Fig. 3(c)) has slightly better lateral resolution but the axial resolution is drastically reduced. The resolution is enhanced when the Wiener filter is applied in both SWF-PB and CWF-PB beamformers, as their imaging results show in Figs. 3(d) and (e), respectively. By adding the SNRD-CF, we can also improve the imaging contrast, as shown in (in Fig. 3(f)).

To enable detailed comparison, we plot the lateral responses for each beamformer at 34 mm, 39 mm, and 44 mm in Figs. 4, where it shows the Dynamic focusing has the worst lateral resolution. Using spatial filters has slightly improved the lateral resolution compared to the coherent PB. The axial responses of three scatterers at 34 mm, 39 mm, and 44 mm are plotted in Figs. 5. On the figures, the SMF-PB is shown to have the worst axial resolution while the SWF-PB has the highest resolution. The resolutions of CWF-PB + SNRD-CF and CWF-PB are both slightly lower than that of the SWF-PB and on par with each other. At each depth, we measure the average beamwidth at -6 dB (full width half maximum (FWHM)), and summarize the results in Table 1. The table also contains the CRs and gCNRs calculated on the hypoechoic lesion for each beamformed image. In the table, the CR measured for the CWF-PB + SNRD-CF is the highest while that calculated for the SMF-PB is the lowest. By using the gCNR, the CWF-PB + SNRD-CF still has the highest contrast ratio while that obtained with dynamic focusing is the lowest.

3.3. Phantom Study

We evaluate the beamformers on data acquired from scanning a multipurpose multi-tissue phantom (Model 040, CIRS Inc., Norfolk, VA, USA). The scan settings are described in Section 3.1. The phantom has a sound-speed of 1540 ± 10 m/s, and its attenuation coefficient slope is -0.5 $\mathrm{dB} \cdot \mathrm{cm}^{-1} \cdot \mathrm{MHz}^{-1}$. The scanned region includes seven wire-targets 80 μm in diameter and two hyperechoic circular lesions 8 mm in diameter, centered at a depth of approximately 30 mm. The contrast of the two hyperechoic lesions is about 15 dB and 6 dB, respectively.

The images generated by the beamformers are showed in Figs. 6. In the figures, all pixel-based beamformed images are generated with data from 32 transmits. The transmit focal depth is at 25 mm. We still use pulses $m_p\left(\mathbf{x}_p, \mathbf{x}_j, t\right)$ and $p_r\left(\mathbf{x}_f, \mathbf{x}_j, t\right)$ simulated with Field II to construct the matched and Wiener filters, but they are generated with a -0.5 $\mathrm{dB} \cdot \mathrm{cm}^{-1} \cdot \mathrm{MHz}^{-1}$ attenuation that is matched to the attenuation of the tissue-mimicking material inside the phantom. The WF-based beamformers are generated with Γ equal to 0.5% of the peak value of the data, and the SNRD-CF is calculated with $\alpha = 5$ and $\beta = \pi$.

Unlike the simulated results, the SMF-PB showed in Fig. 6(c) has a lateral resolution on a par or even worse than that of the coherent PB in Fig. 6(b). This shows the degradation of image quality that results when the impulse response used to construct the filters is no longer exact. The SWF-PB in Fig. 6(d) still show some improvement in axial resolution but the gain is not significant compared to that in the simulation. Meanwhile, the CWF-PB still maintains good performance on the entire imaging region with the imaging result in Fig. 6(e). A significant improvement in imaging contrast is observed in Fig. 6(f) when we combine the CWF-PB with the SNRD-CF.

To study the performance of the various beamformers in more detail, we plot in Figs. 7 and the Figs. 8 responses of each beamformer for three wire-targets A, B, and C, indicated in Fig. 6(b). We measure the FWHMs of each response (in both the axial and lateral directions) and summarize the results in Table. 2. We also calculate the CRs, gCNRs, and eSNRs for each beamformer and present them in the table. The CR and gCNR is calculated on the left lesion

Table 1
Performance metrics on simulation data.

Beamformer	FWHM (Lateral, mm) at			FWHM (Axial, mm) at			CR	gCNR
	34mm	39mm	44mm	34mm	39mm	44mm		
Dynamic focusing	0.661	0.768	0.822	0.606	0.641	0.629	0.408	0.810
Coherent PB	0.448	0.448	0.434	0.608	0.610	0.623	0.450	0.911
SMF-PB	0.398	0.398	0.438	0.775	0.793	0.808	0.374	0.864
SWF-PB	0.349	**0.390**	0.433	**0.384**	**0.400**	**0.398**	0.488	0.868
CWF-PB	0.402	0.440	0.438	0.400	0.406	0.410	0.496	0.888
CWF-PB + SNRD-CF	**0.339**	0.410	**0.400**	0.403	0.403	0.400	**0.917**	**0.925**

(positioned at −2 mm in the lateral direction), while the eSNR is calculated over five beamformed RF frames from the same scanning scene. The image areas used to calculate these metrics are marked in Fig. 6(a). In the table, the proposed method CWF-PB + SNRD-CF has the highest CR and gCNR while the highest eSNR is obtained with the SMF-PB.

3.4. *In Vivo* Study

We conducted a limited study on *in-vivo* data to show the robustness of our proposed CWF-PB + SNRD-CF method to phase aberrations. The data is acquired from an ultrasound carotid scanning from a 23-year-old healthy volunteer using the Verasonics system. The experiment is conducted with appropriate ethical clearance and informed consent. Fig. 9(a) shows the image generated with Dynamic focusing, with a cross-sectional view of the internal jugular vein (IJV), the common carotid artery (CCA), and surrounding structures. The transmit focal depth is at 25 mm. We applied the other beamformers to the data and show the results in Figs. 9(b)-(f). The same pulses $m_p\left(\mathbf{x}_p, \mathbf{x}_j, t\right)$ and $p_r\left(\mathbf{x}_f, \mathbf{x}_j, t\right)$ in the phantom study were used for the *in vivo* study. The WF-based beamformers were configured with Γ equal to

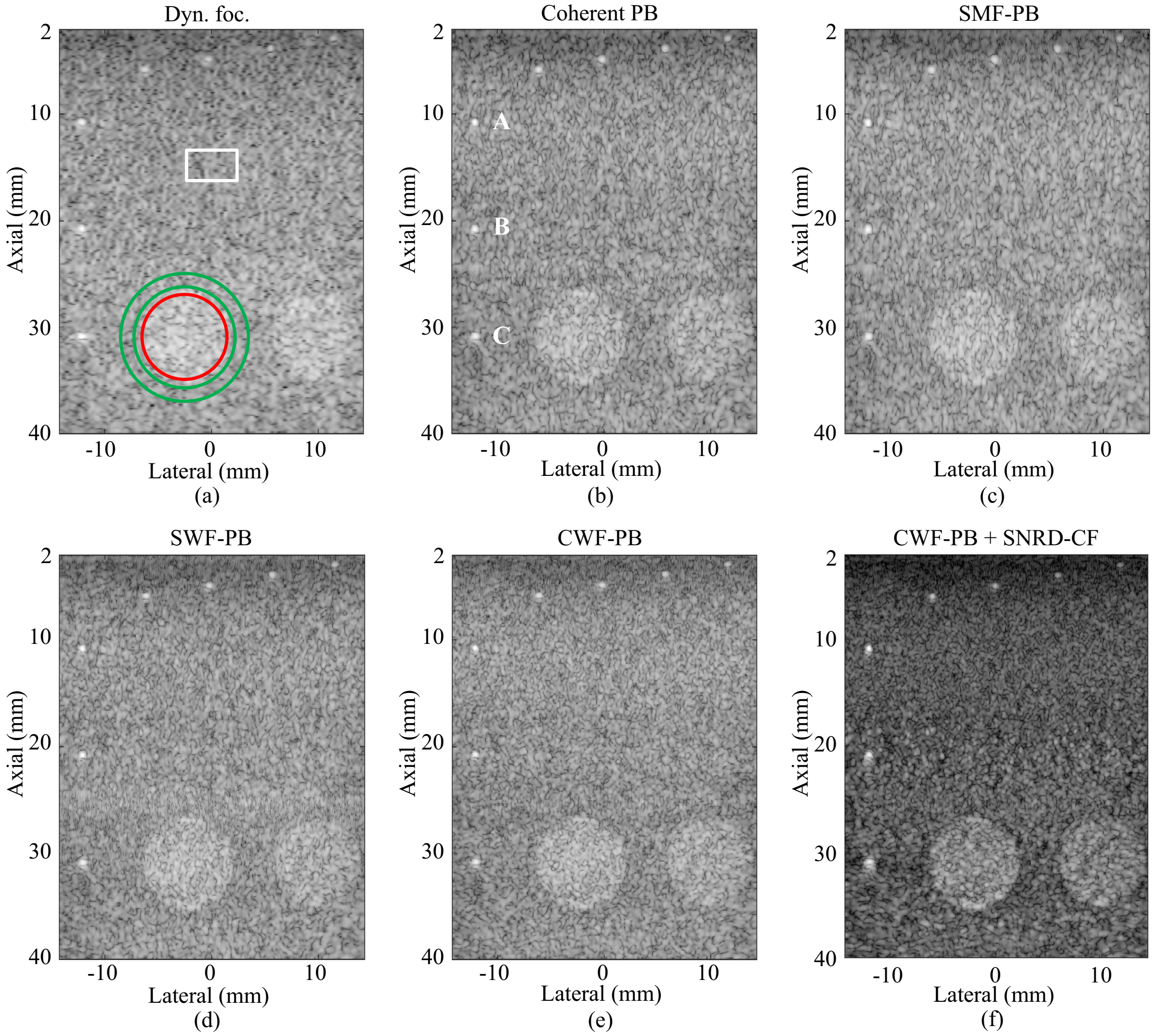

Fig. 6: Images of two idealized hyperechoic lesions and seven wire-targets generated with different beamforming strategies, including (a) Dynamic focusing (Dyn. foc.), (b) Coherent PB, (c) SMF-PB, (d) SWF-PB, (e) CWF-PB, (f) CWF-PB + SNRD-CF. All pixel-based images are generated with data from 32 transmits. They are log-compressed and displayed with a dynamic range of 70 dB. The regions inside the red circle and between the green rings are the kernels used for the computation of CR and gCNR. The region inside the white box is the kernel used for the computation of eSNR.

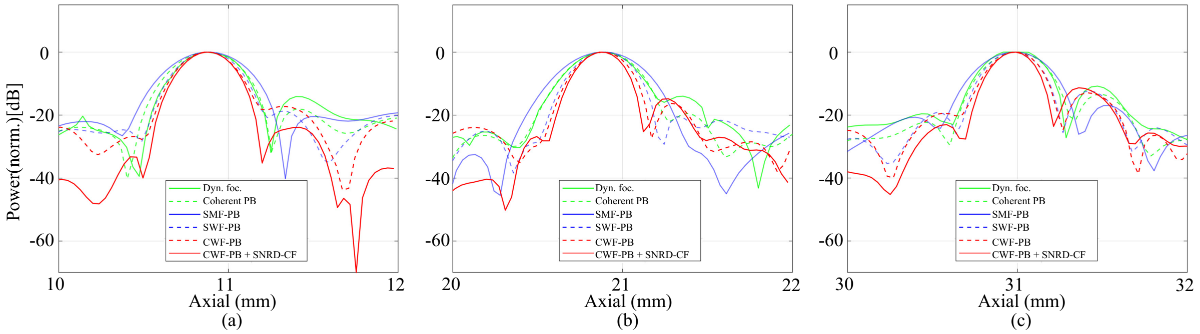

Fig. 7: The axial responses of different beamformers to wire-targets A, B, and C indicated in Fig. 6(b). The beamformers include Dynamic focusing (Dyn. foc.), Coherent PB, SMF-PB, SWF-PB, CWF-PB, and CWF-PB with the SNRD-CF.

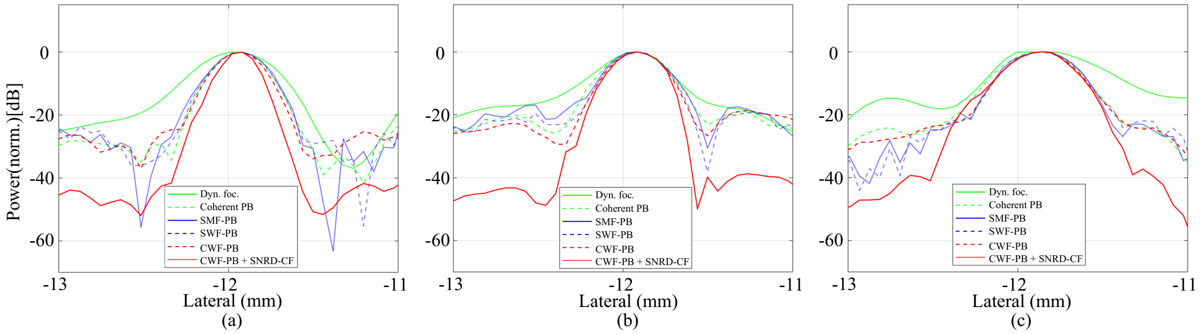

Fig. 8: The lateral responses of different beamformers to wire-targets A, B, and C indicated in Fig. 6(b). The beamformers include Dynamic focusing (Dyn. foc.), Coherent PB, SMF-PB, SWF-PB, CWF-PB, and CWF-PB with the SNRD-CF.

Table 2
Performance metrics on experimental data.

Beamformer	FWHM (Lateral, mm) at A	B	C	FWHM (Axial, mm) at A	B	C	CR	gCNR	eSNR (dB)
Dynamic focusing	0.497	0.442	0.665	0.404	0.420	0.400	0.111	0.565	22.34±6.43
Coherent PB	0.345	0.394	0.468	0.439	0.432	0.401	0.122	0.573	22.83±6.16
SMF-PB	0.357	0.384	0.467	0.496	0.503	0.454	0.123	0.594	**23.01±6.28**
SWF-PB	0.345	0.368	0.453	0.393	0.381	0.350	0.120	0.559	22.43±7.27
CWF-PB	0.322	0.359	0.437	0.365	0.343	0.328	0.140	0.604	21.87±5.88
CWF-PB + SNRD-CF	**0.247**	**0.340**	**0.428**	**0.345**	**0.307**	**0.291**	**0.262**	**0.640**	21.54±5.32

0.5% of the peak value of the data, and $\alpha = 10$ and $\beta = \pi$ were used to derive the SNRD-CF.

Similar to the phantom study, the CWF-PB + SNRD-CF method is showed to have the best performance both in terms of axial resolution and imaging contrast. In contrast, the quality of images generated with SMF-PB and SWF-PB is further reduced on the *in-vivo* data. By comparing the CWF-PB and CWF-PB + SNRD-CF images, we can see the positive effect of using the coherence factor. It helps enhance the IJV edges, indicated by the white arrows in Figs. 9(e) and (f). To observe the benefits of the SNRD-CF more clearly, we magnify a portion of the CCA in each image and show them in Figs. 10. In Figs. 10(c)–(e), there are unwanted artifacts inside the CCA caused by the filtering processes, which degrade the contrast inside the artery lumen. By combining the CWF-PB with the SNRD-CF, we are able to suppress these artifacts as showed in Fig. 10(f).

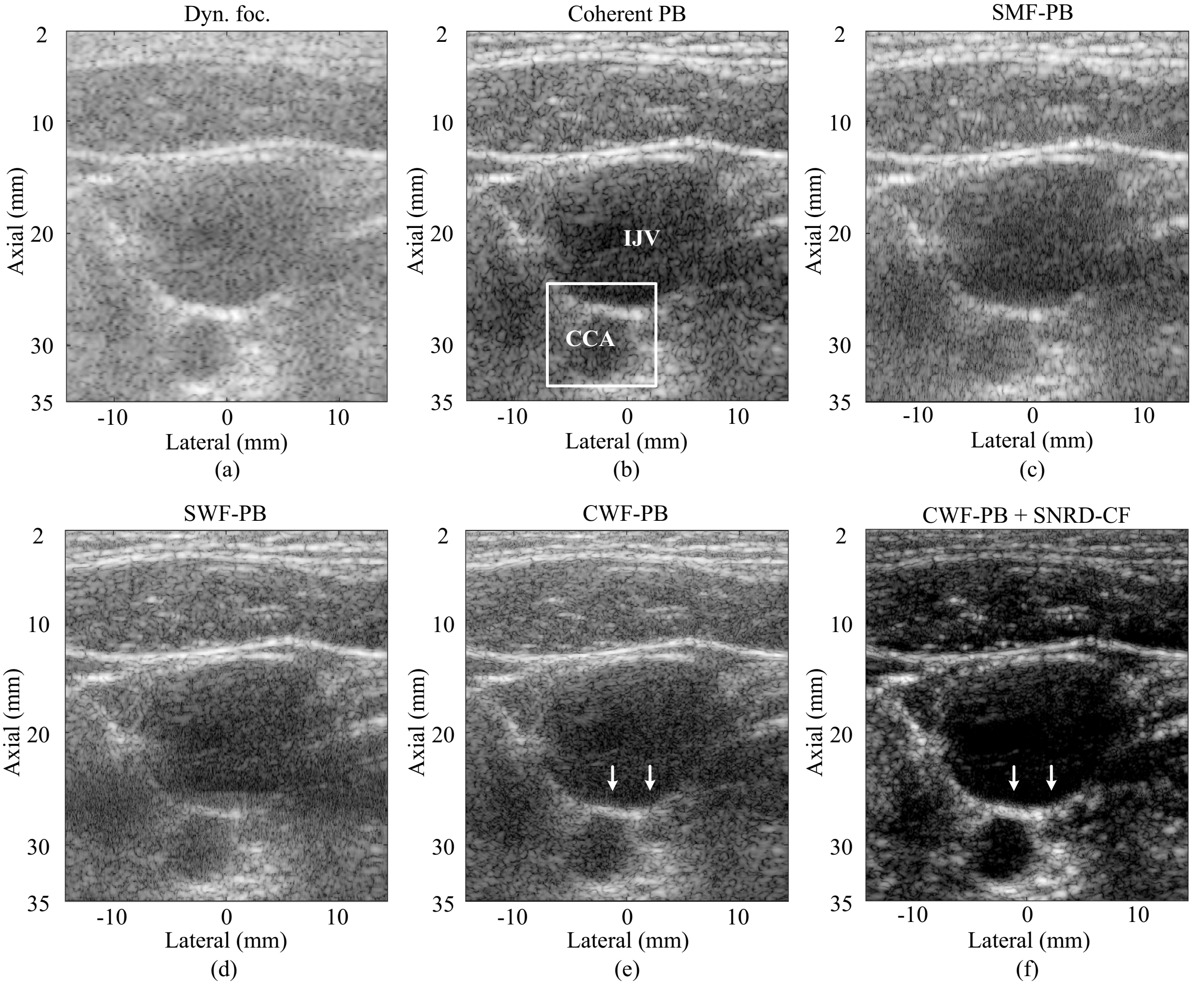

Fig. 9: B-Mode images of the internal jugular vein (IJV) in a transverse view. The images are generated and displayed using (a) Dynamic focusing (Dyn. foc.), (b) Coherent PB, (c) SMF-PB, (d) SWF-PB, (e) CWF-PB, (f) CWF-PB + SNRD-CF. Labels in (b) are also relevant to the corresponding regions in other images. All pixel-based images are generated with data from 32 transmits. They are log-compressed and displayed with a dynamic range of 70 dB.

4. Discussion

The coherent PB beamformer is developed by assuming the received waveforms from individual scatterers include two spherical pulses. Although this model helps extract high-energy signals for the data compounding, it does not take into account the blurring effects caused by the shape of transducer elements and the excitation pulse. Spatial filters, therefore, can be used to incorporate this information into the beamforming process. Such a filter may be applied before the delay-and-sum stage in order to recover the focusing of the echo signals.

In all the experiments of our study, the matched filter is found to broaden the axial resolution of the PB beamformer. Unlike in SA imaging, the filter impulse response for the PB beamformer is constructed from the scan of a scatterer with a focused beam. The response includes two pulses that may be temporally far from each other, especially when the scatterer is located at the edge of the beam. Although the matched filter still maximizes the signal energy at the peak of the response, the long pulse $m_p\left(\mathbf{x}_p, \mathbf{x}_j, t\right)$ increases the sidelobes in the axial direction. As a result, it degrades the range resolution and affects the image contrast.

Compared to the SMF-PB, the Wiener filter kernel in the SWF-PB helps re-focus the data. It is developed based on the linear-shift invariant assumption but the kernel is estimated for each individual imaging pixel. As a result, the

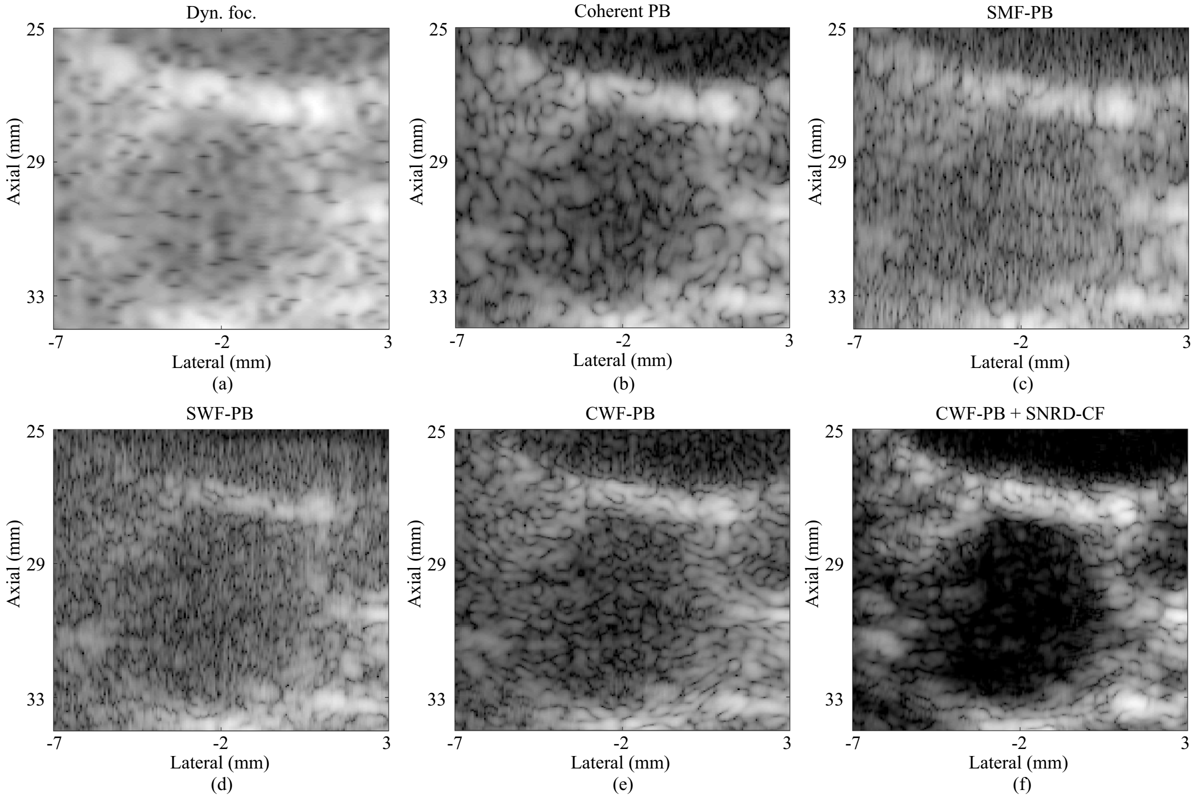

Fig. 10: Magnified views of the regions enclosed by the white rectangles in the images of Fig. 7(b). All images are log-compressed and displayed with a dynamic range of 70 dB.

method offers the best axial resolution in the simulation where each kernel is known exactly. Meanwhile, the Wiener filter in CWF-PB does not focus the signal energy at the center peak. From Eqs. (9) and (11) in our analysis, it is shown that this Wiener filter draws the signal energy from the two pulses of the transmit wave-shape. Thus, the coherent PB beamforming, applied after this filtering process, still plays an important role in selecting the high-energy signals and creating a high-resolution artifact-free B-mode image. In the simulation, the CWF-PB is shown to have a slightly lower axial resolution but at a comparable level to the performance of the SWF-PB. Beside, the diagram in Fig. 2 clearly shows the CWF-PB has less complexity and computational load than the SWF-PB. In particular, the SWF-PB requires one deconvolution at each imaging point. By contrast, the $p_r\left(\mathbf{x}_f, \mathbf{x}_j, t\right)$ in our proposed CWF-PB can be used as a kernel applied at all imaging points, leading to a massive reduction in computation.

In the phantom study, the imaging results show a considerable reduction in the performance of the SWF-PB. A major difference between the simulation and this study is that the pulses $m_p\left(\mathbf{x}_p, \mathbf{x}_j, t\right)$ are no longer known exactly. Several physical uncertainties in the Verasonics system make it difficult to model these pulses accurately. Such modeling errors degrade the axial resolution especially in the far-field. In this region, the actual pulses $m_p\left(\mathbf{x}_p, \mathbf{x}_j, t\right)$ experience noise and ultrasound attenuation, which is hard to replicate reliably in simulation. Although the simulation of the impulse response $p_r\left(\mathbf{x}_f, \mathbf{x}_j, t\right)$ is still subjected to the same unknown noise and varying attenuation, the experiment results show that the improvements of the CWF-PB over the coherent PB is still maintained. Thus, the CWF-PB performance appears to be less sensitive to modeling errors than the SWF-PB.

Similar to the 2-D Wiener filters implemented in our previous studies [11, 32], the CWF-PB does not have much positive impact on the imaging contrast. Improvements in contrast resolution usually require additional signal-processing. In this study, we enhance the contrast by combining the beamformer output with the SNRD-CF in [18]. In our experiments, it is shown to not only improve the imaging contrast but also the axial resolution. This is because the Wiener filter is actually an inverse filter, thus, there are some out-of-phase artifacts that can arise in the filtering process. Combining this with the SNRD-CF, therefore, can suppress such artifacts and improve image quality, especially in relation to the imaging contrast. In this study, we used an adaptive SNRD-CF that responds to the signal and noise power at individual pixels. This helps to avoid dark artifacts generated around hyperechoic lesions caused by using the standard CF [25].

Future work could involve better measurement of the pulses $m_p\left(\mathbf{x}_p, \mathbf{x}_j, t\right)$ and $p_r\left(\mathbf{x}_f, \mathbf{x}_j, t\right)$ to improve the design of the Wiener filter for real data. Our study has shown the strong dependence of beamformer performance on the accuracy of these measurements, especially for the SWF-PB. Unfortunately, errors are unavoidable because of variability in the bio-mechanical properties of the media being scanned and difficulties in characterizing the response of the elements of the ultrasound system. Minimizing these errors will require sophisticated calibration and signal processing techniques. This work remains for further investigation in the next stage of the study.

5. Summary

We have developed a new Wiener filter to improve the axial resolution of pixel-based beamforming. It is based on an extension of our field pattern analysis and serves as a pre-processing filter before the coherent PB beamformer. The output is combined with a SNR-dependent coherence factor for contrast enhancement and to suppress out-of-phase artifacts arising from the Wiener filter. We have demonstrated the new strategy on simulations, experimental and *in vivo* data. The results show improvements in axial resolution, imaging contrast and lesion detectability over the coherent PB approach, while keeping the lateral resolution and eSNR at an equivalent level. The proposed approach is also more robust to modeling errors and more computationally efficient than the other spatial filters evaluated. The simplicity of the Wiener filter when applied to pixel-based beamforming, as well as its good performance in both phantom and *in vivo* experiments, show the potential of using this filter in clinical applications.

Acknowledgment

This work was partially supported by the Fundamental Research Funds for the Central Universities, and the National Natural Science Foundation of China (NSFC61771130).

References

[1] K. E. Thomenius, Evolution of ultrasound beamformers, in: Proceedings of the IEEE Ultrasonics Symposium, IEEE, 1996, pp. 1615–1622.

[2] J. A. Jensen, H. Holten-Lund, R. T. Nilsson, M. Hansen, U. D. Larsen, R. P. Domsten, B. G. Tomov, M. B. Stuart, S. I. Nikolov, M. J. Pihl, Y. Du, J. H. Rasmussen, M. F. Rasmussen, SARUS: A synthetic aperture real-time ultrasound system, IEEE transactions on ultrasonics, ferroelectrics, and frequency control 60 (2013) 1838–1852.

[3] N. Q. Nguyen, R. W. Prager, High-resolution ultrasound imaging with unified pixel-based beamforming, IEEE transactions on medical imaging 35 (2016) 98–108.

[4] N. Q. Nguyen, R. W. Prager, Ultrasound pixel-based beamforming with phase alignments of focused beams, IEEE Transactions on Ultrasonics, Ferroelectrics, and Frequency Control 64 (2017) 937–946.

[5] Y. Lee, W. Y. Lee, C.-E. Lim, J. H. Chang, T.-K. Song, Y. Yoo, Compounded direct pixel beamforming for medical ultrasound imaging, IEEE transactions on ultrasonics, ferroelectrics, and frequency control 59 (2012) 572–582.

[6] C. Yoon, Y. Yoo, T.-k. Song, J. H. Chang, Pixel based focusing for photoacoustic and ultrasound dual-modality imaging, Ultrasonics 54 (2014) 2126–2133.

[7] J. F. Cruza, J. Camacho, R. Mateos, C. Fritsch, A new beamforming method and hardware architecture for real time two way dynamic depth focusing, Ultrasonics 99 (2019) 105965.

[8] J. Chen, E. Wu, H. Wu, H. Zhou, K. Yang, Enhancing ultrasonic time-of-flight diffraction measurement through an adaptive deconvolution method, Ultrasonics 96 (2019) 175–180.

[9] J. Ng, R. Prager, N. Kingsbury, G. Treece, A. Gee, Modeling ultrasound imaging as a linear, shift-variant system, IEEE transactions on ultrasonics, ferroelectrics, and frequency control 53 (2006) 549–563.

[10] H. Gomersall, D. Hodgson, R. Prager, N. Kingsbury, G. Treece, A. Gee, Efficient implementation of spatially-varying 3-d ultrasound deconvolution, IEEE transactions on ultrasonics, ferroelectrics, and frequency control 58 (2011) 234–238.

[11] N. Q. Nguyen, C. K. Abbey, M. F. Insana, An adaptive filter to approximate the bayesian strategy for sonographic beamforming, IEEE Transactions on medical imaging 30 (2010) 28–37.

[12] T. Taxt, J. Strand, Two-dimensional noise-robust blind deconvolution of ultrasound images, IEEE transactions on ultrasonics, ferroelectrics, and frequency control 48 (2001) 861–866.

[13] O. V. Michailovich, D. Adam, A novel approach to the 2-d blind deconvolution problem in medical ultrasound, IEEE transactions on medical imaging 24 (2005) 86–104.

[14] J. Duan, H. Zhong, B. Jing, S. Zhang, M. Wan, Increasing axial resolution of ultrasonic imaging with a joint sparse representation model, IEEE transactions on ultrasonics, ferroelectrics, and frequency control 63 (2016) 2045–2056.

[15] J. A. Jensen, P. Gori, Spatial filters for focusing ultrasound images, in: Proceedings of the IEEE Ultrasonics Symposium, volume 2, IEEE, 2001, pp. 1507–1511.

[16] K.-S. Kim, J. Liu, M. F. Insana, Efficient array beam forming by spatial filtering for ultrasound b-mode imaging, Journal of the acoustical society of america 120 (2006) 852–861.

[17] J. Opretzka, M. Vogt, H. Ermert, A model-based synthetic aperture focusing technique for high-frequency ultrasound imaging, in: 8th European Conference on Synthetic Aperture Radar, VDE, 2010, pp. 1–4.

[18] Y.-H. Wang, P.-C. Li, SNR-dependent coherence-based adaptive imaging for high-frame-rate ultrasonic and photoacoustic imaging, IEEE transactions on ultrasonics, ferroelectrics, and frequency control 61 (2014) 1419–1432.

[19] J. A. Jensen, N. B. Svendsen, Calculation of pressure fields from arbitrarily shaped, apodized, and excited ultrasound transducers, IEEE transactions on ultrasonics, ferroelectrics, and frequency control 39 (1992) 262–267.

[20] C. H. Frazier, W. D. O'Brien, Synthetic aperture techniques with a virtual source element, IEEE transactions on ultrasonics, ferroelectrics, and frequency control 45 (1998) 196–207.

[21] M.-H. Bae, M.-K. Jeong, A study of synthetic-aperture imaging with virtual source elements in b-mode ultrasound imaging systems, IEEE transactions on ultrasonics, ferroelectrics, and frequency control 47 (2000) 1510–1519.

[22] K. W. Hollman, K. W. Rigby, M. O'Donnell, Coherence factor of speckle from a multi-row probe, in: Proceedings of the IEEE Ultrasonics Symposium, IEEE, 1999, pp. 1257–1260.

[23] P.-C. Li, M.-L. Li, Adaptive imaging using the generalized coherence factor, IEEE transactions on ultrasonics, ferroelectrics, and frequency control 50 (2003) 128–141.

[24] B. M. Asl, A. Mahloojifar, Minimum variance beamforming combined with adaptive coherence weighting applied to medical ultrasound imaging, IEEE transactions on ultrasonics, ferroelectrics, and frequency control 56 (2009) 1923–1931.

[25] C.-I. C. Nilsen, S. Holm, Wiener beamforming and the coherence factor in ultrasound imaging, IEEE transactions on ultrasonics, ferroelectrics, and frequency control 57 (2010) 1329–1346.

[26] S. Shamekhi, V. Periyasamy, M. Pramanik, M. Mehrmohammadi, B. Mohammadzadeh Asl, Eigenspace-based minimum variance beamformer combined with sign coherence factor: Application to linear-array photoacoustic imaging, Ultrasonics 108 (2020) 106174.

[27] Y. Wang, H. Peng, C. Zheng, Z. Han, H. Qiao, A dynamic generalized coherence factor for side lobe suppression in ultrasound imaging, Computers in biology and medicine 116 (2020) 103522.

[28] M. Karaman, P.-C. Li, M. O'Donnell, Synthetic aperture imaging for small scale systems, IEEE transactions on ultrasonics, ferroelectrics, and frequency control 42 (1995) 429–442.

[29] A. Rodriguez-Molares, O. M. H. Rindal, J. D'hooge, S.-E. Måsøy, A. Austeng, M. A. L. Bell, H. Torp, The generalized contrast-to-noise ratio: a formal definition for lesion detectability, IEEE transactions on ultrasonics, ferroelectrics, and frequency control 67 (2019) 745–759.

[30] N. Bottenus, B. C. Byram, D. Hyun, Histogram matching for visual ultrasound image comparison, IEEE transactions on ultrasonics, ferroelectrics, and frequency control 68 (2021) 1487–1495.

[31] P. Tortoli, L. Bassi, E. Boni, A. Dallai, F. Guidi, S. Ricci, Ula-op: An advanced open platform for ultrasound research, IEEE transactions on ultrasonics, ferroelectrics, and frequency control 56 (2009) 2207–2216.

[32] N. Q. Nguyen, R. W. Prager, M. F. Insana, Improvements to ultrasonic beamformer design and implementation derived from the task-based analytical framework, Journal of the acoustical society of america 141 (2017) 4427–4437.